ISSN 1063-7745, Crystallography Reports, 2025, Vol. 70, No. 5, pp. 681–686. © Pleiades Publishing, Inc., 2025.

DIFFRACTION AND SCATTERING OF IONIZING RADIATIONS

A New Method of Phase-Contrast Microscopy of Microobjects Using a Nanofocusing Lens in Synchrotron Radiation

M. S. Folomeshkin[a,*], V. G. Kohn[a], A. Yu. Seregin[a], Yu. A. Volkovsky[a], A. V. Aleksandrov[a], P. A. Prosekov[a], V. A. Yunkin[b], A. A. Snigirev[c], Yu. V. Pisarevsky[a], A. E. Blagov[a], and M. V. Kovalchuk[a]

[a] *National Research Centre "Kurchatov Institute," Moscow, 123182 Russia*

[b] *Institute of Microelectronics Technology and High Purity Materials, Russian Academy of Sciences, Chernogolovka, Moscow oblast, 142432 Russia*

[c] *Immanuel Kant Baltic Federal University, Kaliningrad, 236016 Russia*

**e-mail: folmaxim@gmail.com*

Received July 7, 2025; revised July 7, 2025; accepted July 21, 2025

Abstract—The first results obtained by a new experimental method for phase-contrast microscopy of microobjects using synchrotron radiation and a nanofocusing lens in a cone-beam geometry are presented. In the experiment, a secondary radiation source is formed in the lens focus located at a small distance from the microobject, enabling the acquisition of its magnified image. Under the near-field regime, the microobject structure can relatively easily be determined from the experimental image using the transport of intensity equation. The experiment was performed at the KISI-Kurchatov synchrotron radiation source. A model weakly absorbing microobject—commercially available carbon fiber of grade VMN-4—was used. The obtained fiber dimensions and structural features, resolved with submicron spatial resolution, are consistent with the electron microscopy data.

DOI: 10.1134/S1063774525601200

INTRODUCTION

Methods of coherent X-ray microscopy are widely used to visualize the internal structure of microobjects on modern synchrotron radiation (SR) sources. The coherence of an SR beam makes it possible to analyze the structure of weakly absorbing objects, the investigation of which by absorption microscopy is difficult or even impossible. The task of developing new coherent methods of study is urgent in view of the construction of fourth-generation SR sources in Russia [1]. The most popular X-ray method of coherent visualization is phase-contrast microscopy (PCM) [2, 3], where the phase shift of the radiation wave function in the material of studied object is transformed into the intensity contrast for the SR propagating in empty space.

The character of intensity distribution on a detector is determined by the wavelength λ, object size D, and the distance Z after the object. The simplest PCM version implies measurements at relatively small distances (near-field regime), where the condition $D^2 >> \lambda Z$ is fulfilled. In this case, an intensity contrast arises near the boundaries of regions with different optical densities, which often provides information about the object without any complex calculations. At the same time, the near-field approach has two fundamental limitations.

The first one is related to the fact that the resolution of modern area detectors (~0.5 μm) is insufficient for detailed visualization of object with sizes ~1 μm. This problem can be overcome by magnifying an image in a cone-beam geometry of the experiment, when a secondary small-sized SR source is generated before a sample studied. Previously, a scheme was proposed (theoretically considered in [4, 5] and experimentally implemented in [6]), which is based on a nanofocusing compound refractive lens (NCRL) [7, 8]. It was shown that, using NCRL, one can visualize the structure of periodic microobjects with a period less than 0.5 μm, even for an SR beam with a limited spatial coherence.

The second limitation is as follows. To obtain quantitative information about the distribution of object thickness or electron density, one must calculate the phase shift from the measured SR intensity distribution. In the near-field regime, methods based on solving the transport of intensity equation (TIE) are widely used to this end [9–12]. In the general case, a numerical solution of TIE makes it possible to calculate the transverse phase distribution from the measured values of relative SR intensity and its first derivative with respect to the longitudinal coordinate z. However, when using some assumptions (for example, the absence of absorption), only the transverse inten-

sity distribution can be used for phase reconstruction. The solution of the inverse PCM problem using TIE is characterized by simplicity of realization, because is reduced to numerical solution of the Poisson equation with application of the fast Fourier transform algorithm.

In this paper, we present successful implementation of quantitative phase-contrast visualization of weakly absorbing microobjects using TIE in a cone-beam experimental scheme based on NCRL. The TIE applicability for solving the PCM inverse problem using a secondary SR source in the NCRL focus is analyzed. The reported results were obtained on the KISI-Kurchatov source using a model small weakly absorbing microobject and a cone-beam experimental scheme in the near-field regime.

THEORY

The PCM experimental scheme generally contains an SR source, a monochromator, a microobject under study, and a detector; all these elements are aligned along the optical axis (z axis of the coordinate system). The SR source is located at a distance of 10–100 m from the microobject and has finite sizes in the plane oriented perpendicular to the optical axis (x, y); different source points radiate incoherently. The SR is monochromatized using a double-crystal monochromator, which selects a certain wavelength λ from the spectrum, without changing the SR propagation direction. Therefore, its influence can be disregarded, assuming that the microobject is illuminated by monochromatic radiation from different source points independently. The intensity distribution after the microobject is recorded by a high-resolution area detector.

Theoretically, the standard scheme with a finite distance from the source to the object can be reduced to scaling the results for an infinitely remote source, i.e., for an incident plane wave with an intensity I_0. Therefore, it is convenient to consider this case first. We assume that the microobject has a homogeneous composition with the refractive index $n = 1 - \delta + i\beta$, where δ and β describe, respectively, the phase shift and the decrease in the modulus of the SR wave function because of the absorption. The microobject thickness along the z axis depends on the transverse coordinates and is described by a function $t(x, y)$. The case of uniform thickness and transverse dependence $n(x, y)$ is equivalent.

In the geometric optics approximation [13], the SR relative intensity directly behind the microobject is determined as $I(x, y)/I_0 = \exp[-2k\beta t(x, y)]$, and the wave function phase is $\varphi(x, y) = -k\delta t(x, y)$, where $k = 2\pi/\lambda$. The change in the SR intensity after the microobject along the z axis in the paraxial approximation is described by TIE [9]:

$$\nabla_\perp[I(x, y, z)\nabla_\perp\varphi(x, y, z)] = -k[\partial I(x, y, z)/\partial z], \quad (1)$$

where $\nabla_\perp$ is the gradient operator over the transverse coordinates (x, y). TIE describes the change in the intensity of the radiation propagating behind the object due to the nonuniform phase distribution; it can be used to calculate the phase, which is proportional to the object thickness. To this end, it is necessary to measure the intensity in the plane directly behind the microobject, at the distance z_1 satisfying the near-field condition. In this case, the derivative $\partial I(x, y, z)/\partial z$ can be estimated as a finite difference $\Delta I/z_1$ [12].

Equation (1) is simplified for a microobject with negligible absorption ($k\beta t << 1$):

$$\nabla_\perp^2\varphi(x, y) = -(k/z_1)[I_t(x, y) - 1], \quad (2)$$

where $I_t(x, y) = I_1(x, y)/I_0$, $I_1(x, y)$ is the intensity distribution at the distance z_1 from the microobject and I_0 is the incident radiation intensity. Here, it is sufficient to measure one time the intensity behind the microobject. Expression (2) is the Poisson equation; it can be solved numerically for $\varphi(x, y)$ using the fast Fourier transform algorithm [10–12]. Then, with the known parameter δ, the microobject thickness is calculated as $t(x, y) = -\varphi(x, y)/(k\delta)$. Note that, under the conditions of a real experiment, the intensity I_0 of the incident SR beam is not strictly constant. However, at weak variations in intensity ($\nabla_\perp I_0(x, y) \approx 0$), Eq. (2) can be solved using the measured intensity distribution without a microobject at the distance z_1.

For the real geometry of an experiment with an extended SR source, whose points emit incoherently, the resulting intensity distribution is the sum of the intensity distributions from each source point over all points. In the paraxial approximation, the intensity $I_{z0}(x, y, z)$ for a thin microobject illuminated by a point source at a distance z_0 is related to the intensity $I_\infty(x, y, z)$ for a plane wave by the relation

$$I_{z0}(x, y, z = z_1) = M^{-2}I_\infty(x_e, y_e, z = z_e), \quad (3)$$

where $x_e = x/M$, $y_e = y/M$, $z_e = z_1/M$, and the parameter $M = z_1/z_0 + 1$ is the geometric magnification factor [6, 13]. In other words, the image of a microobject illuminated by a point source is equivalent to the image obtained under illumination by a plane wave, but with a changed scale over the transverse coordinates x_e, y_e and effective propagation distance z_e. This circumstance makes it possible to solve Eq. (2), valid for an incident plane wave, also for a microobject illuminated by a point source, replacing $I_1(x, y)$ and z_1 with $I_{z0}(Mx, My)$ and z_e, respectively.

A displacement of a point source perpendicular to the optical axis to a point with the coordinates x_s, y_s leads to displacement of the image as a whole by the distances $(M - 1)x_s$ and $(M - 1)y_s$ along the x and y axes, respectively. As a result, if the SR source brightness is set by the function $S(x, y)$, the image $I_d(x, y)$ of

a microobject illuminated by an extended source takes the form

$$I_d(x, y) = I_{z0}(x, y) * P(x, y), \quad (4)$$

where $P(x, y) = S(x/[M - 1], y/[M - 1])$ is the function of the source projection onto the image plane. The symbol * denotes two-dimensional convolution. The brightness $S(x, y)$ for SR sources is generally approximated well by a two-dimensional Gaussian function.

Note the evident property of Eq. (2). If $\varphi(Mx, My)$ is a solution for the intensity $I_{z0}(Mx, My)$, the solution for the intensity $I_d(Mx, My)$ from (4) is

$$\varphi_d(Mx, My) = \varphi(Mx, My) * P(Mx, My). \quad (5)$$

It follows from these considerations that the accuracy of the phase image obtained by solving Eq. (2) is determined by the size of the SR source projection. Note that the accuracy also decreases with increasing the distance at which the intensity distribution is recorded, because Eq. (2) is valid only in the near-field approximation. However, numerical calculations show that, even when the near-field criterion is not strictly fulfilled, the phase is determined with a satisfactory accuracy.

The standard geometry of the experiment on a SR source corresponds to the condition $z_0 >> z_1$, and the image is barely magnified, because $M \approx 1$. To obtain a significant magnification, one must use the inverse condition $z_0 << z_1$, corresponding to a cone-beam geometry. In this case, $M \approx M - 1 = z_1/z_0$, and the image scale increases unlimitedly with an increase in z_1. In addition, the near-field criterion is determined by the effective distance $z_e \approx z_0$; i.e., the image character barely depends on z_1. With increasing z_1, the scale of the source projection function $P(x, y)$ increases simultaneously with the image magnification. With allowance for (5), one can see that the resolution of the reconstructed image of the phase $\varphi_d(Mx, My)$ is determined in this scheme directly by the SR source size rather than the source projection.

From a practical point of view, a microobject under study cannot be located close to an SR source. In addition, since the sizes of modern SR sources are 10–100 μm, the source projection size would significantly exceed the image size. These problems can be solved by a new method of SR beam nanofocusing, using a planar NCRL [7, 8] to form a secondary source before the microobject [4–6]. The experimental scheme of PCM based on a planar NCRL is presented in Fig. 1.

Planar NCRLs consist of many identical focusing elements. The refracting surface of the elements is a parabolic cylinder, which provides linear focusing in one plane. Modern silicon NCRLs with an aperture of 50 μm are characterized by a high manufacturing accuracy and provide focusing of a coherent SR beam to a transverse size of less than 50 nm [14]. The analytical theory of SR focusing using NCRLs was developed in [15–19]. The SR focusing can be calculated based on the equations of the developed theory using the available XRWP program [20], as well as the online-program [21], which makes it possible to calculate the focused-beam parameters.

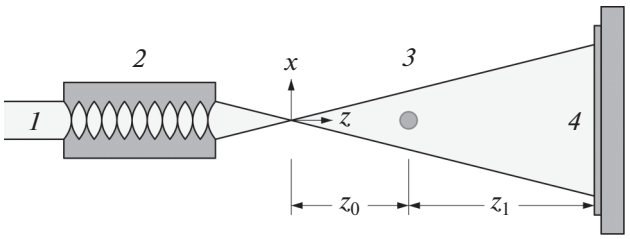

Fig. 1. Experimental PCM scheme using a planar NCRL: (*1*) monochromatic SR beam, (*2*) NCRL, (*3*) microobject, and (*4*) detector.

It follows from the theory that the wave function of focused radiation for strongly absorbing CRLs is a Gaussian function, which is characterized by a half-width w_f in the focus and an angular divergence $\Delta\theta$. These parameters are related as follows: $w_f = 0.441(\lambda/\Delta\theta)$. For a sufficiently large distance from the focus, $z_0 >> z_R$, where $z_R = 2.27(w_f/\lambda)$ is the Rayleigh length, the transverse dependence of the phase is parabolic, which corresponds to a point source in the paraxial approximation. This means that an NCRL can be used to magnify the microobject image, similar to a point source. The difference between these two cases is that the finite divergence $\Delta\theta$ must be taken into account for a Gaussian beam to provide complete microobject illumination. The half-width of beam intensity on the sample, w_0, should exceed the sample size to satisfy the uniform illumination condition in (2). For example, for a photon energy $E = 12$ keV ($\lambda = 0.1$ nm), if the beam focal size is $w_f = 50$ nm, the angular divergence $\Delta\theta = 911$ μrad. Then the beam half-width w_0 at the distance $z_0 = 20$ mm is 18 μm, which is sufficient for illuminating a microobject with a characteristic size $D = 10$ μm. The near-field condition $D^2 >> \lambda z_0$ is also fulfilled in this case.

In the case of an extended SR source, its diminished image is formed in the NCRL focus. Each point of the SR source corresponds to a nanosized Gaussian beam in the focus. As was shown in the previous paragraph, each such Gaussian beam can approximately be considered as a point source. Then the secondary SR source can also be considered as a set of incoherently emitting point sources. Thus, with allowance for (5), the resolution of the reconstructed image of the microobject phase is limited by the incoherent size of the secondary SR source in the NCRL focus. Note that this size can be increased in a real experiment due to other factors, for example, vibrations of optical scheme elements.

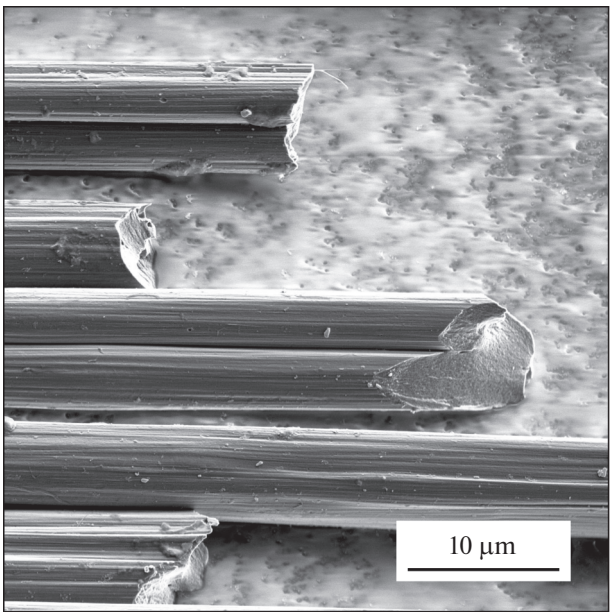

Fig. 2. SEM image of a VMN-4 CF.

EXPERIMENT

The experiment was performed on the X-ray Crystallography and Physical Materials Science (XCPM) beamline of the KISI-Kurchatov source, where SR is generated by a bending magnet located at a distance $z_s = 15$ m from a sample studied. The SR source is approximated by a two-dimensional Gaussian function with half-widths of ~100 μm in the vertical direction and ~1000 μm in the horizontal direction. The SR beam is monochromatized using a double-crystal Si(111) monochromator, whose angular position is tuned to the photon energy $E = 12$ keV. A detailed technical description of the XCPM beamline is presented in [22].

The model sample was commercially available carbon fiber (CF) of grade VMN-4 [23]. Figure 2 presents a scanning electron microscopy (SEM) image of individual CFs. VMN-4 CFs have an approximately elliptical cross section with sizes of ~8 and 5 μm along the major and minor axes, respectively. The average fiber density is ~1.7 g/cm^3. One can also see in Fig. 2 that individual CFs have a characteristic depression over the entire length, which arises as a result of high-temperature annealing. Since the sample studied was a linear microobject, a scheme with one-dimensional magnification in the direction perpendicular to the CF axis was used.

A secondary linear source was formed using a silicon NCRL with an aperture of 50 μm and a number of elements $N = 104$. The NCRL was mounted on a goniometer for spatial and angular positioning when tuning the experimental scheme. Focusing was performed in the vertical plane, corresponding to the minimum SR source size. For the aforementioned experimental parameters, the theoretical value of the coherent beam size in the NCRL focus was $w_f = 68$ nm. This value corresponds to the beam divergence $\Delta\theta = 670$ μrad. The sample was installed on piezoelectric actuators, providing its positioning with a nanometer precision, at the distance $z_0 = 20$ mm after the NCRL focus. With allowance for divergence, the beam half-width at the sample site was $w_0 = 13.4$ μm, which is larger than the CF diameter.

The intensity distribution was recorded using a two-dimensional X-ray detector XSight Micron (Rigaku) based on a scintillation screen and an sCMOS camera. The detector was located at the distance $z_1 = 275$ mm after the sample. For the aforementioned values of z_0 and z_1, the geometric image magnification was $M = 14.75$. In the experiment, we first recorded the empty beam image, i.e., the intensity distribution $I_0(x, y)$ without a sample in order to take into account the phase-contrast image background. Then the sample studied was positioned in the SR beam diverging after the NCRL, and the phase-contrast image $I_1(x, y)$ was recorded.

RESULTS AND DISCUSSION

The magnified images of the empty SR beam after the secondary source, $I_0(x, y)$, and the CF phase contrast, $I_1(x, y)$, are presented in Fig. 3. Since the image is magnified in only the vertical plane, the number of pixels in the vertical direction is larger than along the horizontal. The vertical scale corresponds to the sizes at the sample position, with allowance for Eq. (3). The effective detector pixel size in the vertical direction with allowance for the geometric magnification is 22 nm.

The distribution of the empty beam intensity (Fig. 3a) in the vertical direction is described fairly accurately by a Gaussian function, which corresponds to the analytical theory of NCRL-aided focusing. The insignificant deviations from the ideal Gaussian shape are related to the nonuniform distribution of the SR beam intensity incident on the NCRL. The introduction of a CF into the beam leads to the occurrence of a strong contrast of the intensity distribution in the vertical direction (Fig. 3b). The image is significantly blurred in the horizontal direction because of the relatively large SR source size in this direction and the absence of focusing in the horizontal plane. However, this is not a limitation for a one-dimensional sample, because its thickness is approximately constant along x.

Along with the contrast at the CF boundaries, one can observe an increase in intensity at the image center, which is caused by the gradient of CF thickness in the region of characteristic depression (Fig. 2). Note that, for the photon energy in use, the theoretical absorption in the thickest part of the CF is less than 0.2%; i.e., the CF can be considered an X-ray-trans-

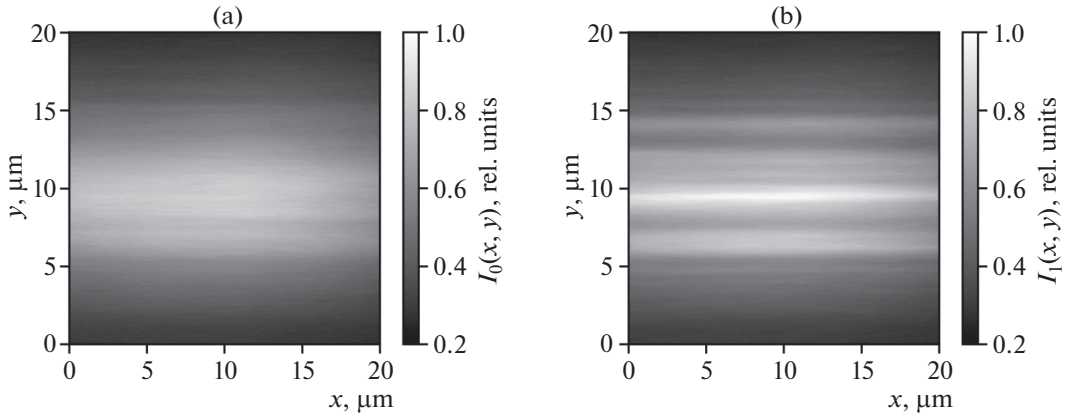

Fig. 3. Recorded images of (a) SR beam after NCRL and (b) CF phase contrast.

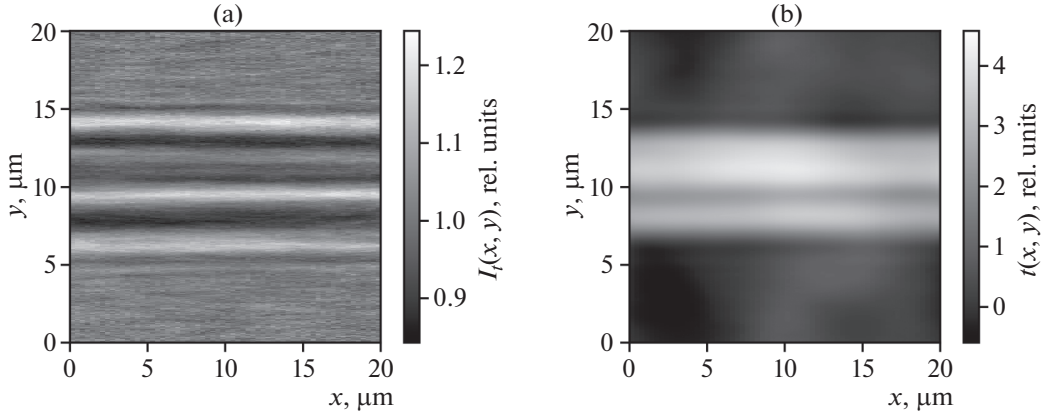

Fig. 4. (a) Intensity distribution used for reconstruction and (b) reconstructed CF thickness distribution.

parent object, and the intensity contrast in Fig. 3b is a purely phase one.

To reconstruct the phase from the measured images, we calculated the function $I_t(x, y) = I_1(x, y)/I_0(x, y)$ in Eq. (2). The image $I_t(x, y)$ is presented in Fig. 4a. One can assume approximately that this image corresponds to the case of an incident plane wave with unit intensity. It can be seen that the image contains a high-frequency background, related to the shot noise during signal detection. Nevertheless, the intensity contrast is sufficiently bright in comparison with the noise level. The phase distribution was reconstructed from the image $I_t(x, y)$ by solving numerically Eq. (2) using the fast Fourier transform algorithm. Then the thickness distribution was calculated as $t(x, y) = -\varphi(x, y)/(k\delta)$.

The reconstructed image $t(x, y)$ is presented in Fig. 4b. One can clearly see CF boundaries, as well as a characteristic depression in the central part. The CF diameter in the image plane is approximately 8.5 μm, which slightly exceeds the real major CF diameter: ~8 μm. The maximum reconstructed thickness along the optical axis is ~4.5 μm at a real value of the minor CF diameter (~5 μm). The increase in size in the image plane and the decrease in thickness can be explained by the image blurring in correspondence with (5), because of the finite size of the secondary source in the NCRL focus. This leads both to blurring of boundaries in the image plane and to reduction of the thickness values $t(x, y)$.

One can observe the presence of artifacts in the form of distortions around the CF in the reconstructed image. These distortions are due to the noise in the phase-contrast image. When solving Eq. (2) using a Fourier transform, high frequencies are amplified, which manifests itself in the form of artifacts in the reconstructed image [11, 12]. These artifacts may distort significantly the reconstruction result. However, when an SR source with a high brightness is applied, this problem is of little importance, because the signal-to-noise ratio is sufficiently large in this case.

As follows from the theory, the accuracy of the image reconstructed using Eq. (2) is determined by the secondary-source incoherent size in the NCRL focus. This size is determined by both the SR source size and the presence of vibrations of experimental setup elements. For the experimental parameters in use, the theoretical beam size in the NCRL focus, with allow-

ance for the finite SR source size, is 100 nm. However, as was shown previously [6, 24], the real beam size in the NCRL focus on the XCPM beamline is ~0.5 μm for the aforementioned parameters because of the existence of vibrations. Thus, the resolution of the reconstructed thickness image is ~0.5 μm; it is limited primarily by the mechanical instability of the experimental setup elements rather than the finite spatial coherence of the SR beam. With this factor excluded, a spatial resolution of ~100 nm can theoretically be achieved even on a second-generation SR source. Implementation of the proposed experimental scheme on a third- or fourth-generation SR source should provide even better resolution.

CONCLUSIONS

The applicability of the transport of intensity equation for quantitative reconstruction of the thickness distribution for an X-ray-transparent microobject by phase-contrast microscopy using a secondary SR source in the focus of a nanofocusing compound refractive lens was demonstrated. It was shown that the spatial resolution of the reconstructed image is determined by the incoherent SR beam size in the lens focus.

An experimental scheme with a silicon lens having an aperture of 50 μm was implemented on the XCPM beamline of the KISI-Kurchatov SR source, and an image of a CF with a diameter of ~8 μm was obtained. This image was reconstructed from experimental data on measuring intensity; it is in agreement with the SEM data. The spatial resolution of the obtained image is ~500 nm. It is limited primarily by the mechanical instability of the experimental setup elements. With this factor excluded, a resolution of ~100 nm can be achieved on a second-generation SR source. The use of the lens on a third- or fourth-generation SR source should theoretically provide even higher resolution.

FUNDING

This study was carried out within the State assignment of NRC "Kurchatov Institute." The work by V.A. Yunkin on fabrication of silicon refracting lenses was supported in part by State assignment no. 075-00295-25-00.

CONFLICT OF INTEREST

The authors of this work declare that they have no conflicts of interest.

REFERENCES

1. M. V. Kovalchuk, A. E. Blagov, O. S. Naraikin, et al., Crystallogr. Rep. **67**, 678 (2022). https://doi.org/10.1134/S1063774522050078
2. A. Snigirev, I. Snigireva, V. Kohn, et al., Rev. Sci. Instrum. **66** (12), 5486 (1995). https://doi.org/10.1063/1.1146073
3. T. S. Argunova and V. G. Kohn, Usp. Fiz. Nauk **189**, 643 (2019). https://doi.org/10.3367/UFNr.2018.06.038371
4. V. G. Kohn, Crystallogr. Rep. **67**, 826 (2022). https://doi.org/10.1134/S106377452206013X
5. V. G. Kohn and T. S. Argunova, Phys. Status Solidi B **259** (4), 2100651 (2022). https://doi.org/10.1002/pssb.202100651
6. M. S. Folomeshkin, V. G. Kohn, A. Yu. Seregin, et al., Crystallogr. Rep. **69**, 787 (2024). https://doi.org/10.1134/S1063774524602429
7. V. Yunkin, M. V. Grigoriev, S. Kuznetsov, et al., Proc. SPIE **5539**, 226 (2004). https://doi.org/10.1117/12.563253
8. A. Snigirev, I. Snigireva, V. Kohn, et al., Phys. Rev. Lett. **103**, 064801 (2009). https://doi.org/10.1103/PhysRevLett.103.064801
9. M. R. Teague, J. Opt. Soc. Am. **73** (11), 1434 (1983). https://doi.org/10.1364/JOSA.73.001434
10. D. Paganin, S. C. Mayo, T. E. Gureyev, et al., J. Microsc. **206** (1), 33 (2002). https://doi.org/10.1046/j.1365-2818.2002.01010.xTomography
11. A. Burvall, U. Lundström, P. A. C. Takman, et al., Opt. Express **19** (11), 10359 (2011). https://doi.org/10.1364/OE.19.010359
12. M. Krenkel, M. Bartels, and T. Salditt, Opt. Express **21** (2), 2220 (2013). https://doi.org/10.1364/OE.21.002220
13. D. M. Paganin, *Coherent X-Ray Optics* (Oxford University Press, New York, 2006).
14. M. S. Folomeshkin, V. G. Kohn, A. Yu. Seregin, et al., Crystallogr. Rep. **68**, 1 (2023). https://doi.org/10.1134/S1063774523010078
15. V. G. Kohn, JETP Lett. **76**, 701 (2002). https://doi.org/10.1134/1.1541043
16. V. G. Kohn, J. Exp. Theor. Phys. **124**, 224 (2003). https://doi.org/10.1134/1.1600812
17. V. G. Kohn, J. Synchrotron Radiat. **25**, 1634 (2018). https://doi.org/10.1107/S1600577518012675
18. V. G. Kohn and M. S. Folomeshkin, J. Synchrotron Radiat. **28**, 419 (2021). https://doi.org/10.1107/S1600577520016495
19. V. G. Kohn, J. Synchrotron Radiat. **29**, 615 (2022). https://doi.org/10.1107/S1600577522001345
20. V. G. Kohn (2024). https://xray-optics.ucoz.ru/XR/xrwp.htm
21. V. G. Kohn (2024). https://kohnvict.ucoz.ru/jsp/1-crl-par.htm
22. V. G. Kohn, P. A. Prosekov, A. Yu. Seregin, et al., Crystallogr. Rep. **64** (1), 24 (2019).
23. Yu. S. Virgil'ev and I. P. Kalyagina, Inorg. Mater. **40** (Suppl. 1), S33 (2004). https://doi.org/10.1023/B:INMA.0000036327.90241.5a
24. M. N. Sorokovikov, D. A. Zverev, A. A. Barannikov, et al., Nanobiotechnol. Rep. **1** (Suppl. 1), S210 (2023). https://doi.org/10.1134/S2635167623601183

Translated by Yu. Sin'kov

SPELL: OK